The ionizing cluster of 30 Doradus

III. Star-formation history and initial mass function[*]

F. Selman[1], **J. Melnick**[1], **G. Bosch**[2], **and R. Terlevich**[2]

[1] European Southern Observatory, Alonso de Córdova 3107, Santiago, Chile
[2] Institute of Astronomy, Madingley Road, Cambridge CB3 0HA, UK

Abstract. A new method is presented and used to determine the IMF of the starburst cluster NGC2070. A new correction, the *magnitude-limit correction* is introduced, and shown to be crucial when attempting to derive the IMF in the presence of variable reddening when the photometry is not several magnitudes deeper than the fainter stars analyzed. Failure to apply this correction is responsible for the drop at the low mass end of the IMF found in previous work on this cluster, despite the proper application of incompleteness corrections. For masses between $3M_\odot \lesssim M \lesssim 120M_\odot$ and outside $15''$ the IMF of NGC2070 is shown to be consistent with being a single power law with a Salpeter exponent. In the central region ($4.6'' < r < 19.2''$) within $2.8M_\odot < M < 120M_\odot$ our data combined with HST observations yield a slope flatter than Salpeter at the 2–3σ level. Furthermore, it is shown that the number of $M > 50M_\odot$ stars near the core (Massey & Hunter 1998a, 1998b) is incompatible with the intermediate mass counts of Hunter et al. (1995, 1996) extrapolated with a Salpeter slope, so either the slope is flatter than Salpeter, or the HST spectral types are biased towards earlier types. The star-formation history is dominated by three bursts of increasing strength occurring 5My, 2.5My, and $\lesssim$1.5My ago, the latest one responsible for most of the star-formation within 6 pc from the cluster center. A spherically symmetric structure is detected at about 6 pc from the cluster center which contains predominantly massive stars and has a flatter IMF. The surface number density profile of the cluster is shown to be well modeled by a single power law, $\Sigma(R) \simeq R^{-\alpha}$, over $0.4\,\mathrm{pc} < R < 12\,\mathrm{pc}$, with $\alpha \approx 1.85$, significantly steeper than isothermal.

Key words: stars: early-type – stars: Hertzsprung–Russel (HR) and C-M diagrams – stars: luminosity function, mass function – ISM: dust, extinction – Galaxy: open clusters and associations: general – galaxies: Magellanic Clouds

1. Introduction

The Initial Mass Function (IMF) of starburst clusters has become critical for our understanding of the Universe at high redshifts. Starbursts are a natural consequence of tidal interactions and merging (e.g. Mihos & Hernquist 1994, and references therein) and there are good reasons to believe that these processes were more frequent in the past (Barnes 1998): first, recent work suggests that the number of pairs of galaxies was larger in the past than it is today (Abraham 1999); second, most of the high z galaxies, as revealed for example by the *Hubble Deep Field* (HDF) can be classified as Irr/Pec/Merger (Glazebrook et al. 1995; Abraham et al. 1996). In addition, the signatures of starbursts have been actually observed at very large redshifts (Pettini et al. 1998). Thus, violent star formation and starburst clusters have gained a new status: a large fraction of the old stellar population of present day galaxies appears to have formed in starbursts. 30 Doradus, as the nearest example of a starburst cluster and the only one whose stellar population can be spatially resolved from the ground, is a natural laboratory for our studies of the IMF of these objects.

Beyond its importance in helping us decode the information contained in the light we receive from distant objects, the IMF is interesting in its own right. In what follows it will be useful to recognize, somewhat arbitrarily, three mass ranges: (1) the low mass end defined by $M < 1M_\odot$; (2) the intermediate mass range defined by $1M_\odot \lesssim M < 20M_\odot$; and (3) the high mass end defined by $20M_\odot \lesssim M < 120M_\odot$. It has recently being proposed that the stellar IMF is the direct result of a random sampling of a fractal molecular cloud system (Elmegreen 1997). In this view the form of the IMF has its origin in the turbulent processes that give molecular clouds their fractal structure, so the intermediate and high mass range IMF is expected to be a universal power law function, $dN \propto M^{-(1+\Gamma)}dM$, with an exponent close to the Salpeter value, $\Gamma = 1.35$ (Salpeter 1955).

Notwithstanding its attractiveness, the idea of universality is contradicted by some observations of clusters in the Large Magellanic Clouds (LMC) and the Milky Way. These observations reveal a mass function subject to important regional variations in the intermediate to high mass range (Parker et al. 1992; Walborn & Parker 1992), variations that have been used to support the idea of propagating or contagious star formation. However, a

proper control over systematic effects is a pre-requisite to properly analyze this type of observations. In this paper, the third in a series of papers studying the IMF and star-formation history of the 30 Doradus superassociation, we develop a method that reduces the magnitude of systematic effects thus permitting the determination of stellar physical parameters in an unbiased way. In particular, we show that a hitherto neglected systematic effect might be responsible for some of the claims of regional variations of the IMF mentioned above.

In Paper I we used *Daophot II* (Stetson 1997; Davis 1994) to analyze a set of UBV frames of 30 Doradus obtained in sub-arcsecond seeing and photometric conditions. The overall completeness limit, defined as the magnitude at which the probability of detection in all three filters equals 50%, was found to be V=19.2. These observations are used, together with the spectroscopy presented in Paper II (Bosch et al. 1999), to determine the reddening law of the region. In this paper we combine the photometry and reddening determination from Paper I with the spectroscopy from Paper II to "read" the star-formation history of the region, and to determine its IMF for almost the full intermediate to high mass range. This will give us the keys to interpret other regions of star formation. Reddening is shown to play a crucial role, as the culprit of a hitherto scarcely described systematic effect, possibly responsible for some of the variations that have been found in the IMF slopes of various systems.

2. From UBV photometry to physical parameters: the colour-magnitude stereogram

The determination of the fundamental physical parameters of massive stars in young clusters from UBV photometry poses a formidable observational challenge (Melnick 1992; Massey 1998). In fact, it has been claimed that the problem is equally challenging even for photometric systems extending into the far UV (Hunter et al. 1997). In Paper I we introduced a new tool, the Color-Magnitude Stereogram (CMS) and we showed how this tool can be used to visualize the different systematic effects that complicate the problem, including the effects of zero point calibrations (especially in the U-band), the effect of variable reddening, etc. In fact, the CMS is much more than just a visualization tool; it also provides possibly the only tool to derive the fundamental stellar parameters (age, effective temperature, luminosity) from UBV magnitudes in the presence of strong and variable reddening. A detailed description of this process is presented below.

2.1. The theoretical surface

The *theoretical surface* in the CMS is the locus of all stars in a reddened cluster in the absence of observational errors. To see this better, consider a cluster of coeval stars. In the three dimensional [(B-V),(U-B),V] space (the CMS) these stars fall on a spatial curve which is the generalization of the corresponding isochrone. In the presence of reddening, these stars are shifted away from the isochrone along a vector which can

be parametrized by $R_V = A_V/E(B-V)$ and $S = E(B-V)/E(U-B)$. If, as is the case for 30 Doradus, the reddening is variable and changes from star to star (see Fig. 7), all stars in the cluster fall on a surface, the *theoretical surface,* which is defined by the theoretical isochrone and the reddening vector $\mathbf{R} = (1, S, R_V)$ times the color excess E(B-V). Thus, the position of a star on the theoretical surface univocally determines the reddening free colors of the star. Two real-life effects complicate this simple picture: the clusters stars are not necessarily coeval, and all observations are affected by measurement errors.

In order to deal with these effects we have developed a process which is in fact a generalization of the standard approach to three dimensions. We start with theoretical isochrones. We have used the Geneva tracks for Z=0.008 appropriate for the LMC as presented by Meynet et al. (1994). These models, which assume twice the standard value for the stellar mass loss rates, are chosen because they reproduce better the observed populations of massive stars in galaxies, but our results are insensitive to this parameter as we will show later. For each initial mass, M_i, the models give effective temperatures (T_{eff}) and radius (R_{eff}) as a function of age (t) in million years. In principle, to convert these parameters to magnitudes and colors atmosphere models are needed. In practice, however, it is much simpler to use semi-empirical[1] conversions from T_{eff} to UBV colors (Schmidt-Kaler 1982, SchK) and T_{eff} to bolometric correction (Chleboswsky & Garmany 1991, ChG; Vacca et al. 1996, VGS; Malagnini et al. 1986). We have collected together these conversion tables in Fig. 1 for comparison and easy reference. Notice that the ChG temperature scale is much cooler than the VGS one. Since the temperature range spanned by the theoretical isochrones reach values much larger than those covered by ChG, their conversion produces a false turn-up in the HR-diagram. Therefore, in this paper we only consider the VGS calibration. For each age, we generate the theoretical surfaces transforming the theoretical isochrones into UBV space through these relations and applying the reddening vector over the full range of color excesses E(B-V) observed in the cluster. Examples of theoretical surfaces are presented in Fig. 2.

For each set of physical parameters we now have a unique set of observable quantities. We now need to solve the inverse problem: given a set of observations of a star, find the most probable combination of initial mass, age, and reddening that would result in that observation. The solution to this problem is well known and involves the use of Bayes theorem together with a model for the observational errors.

2.2. The Bayesian approach

In a Bayesian approach probabilities are assigned to hypothesis such as: *the star formed t years ago, with an initial mass M_i, and is presently reddened by an amount E(B-V).* Using a model of the phenomenon under study together with a model

---

[1] The model atmospheres of Kurucz (1993) were used to determine that, for dwarfs, metallicity effects are not important for the T_{eff}-color conversion in the mass range of interest in this research.
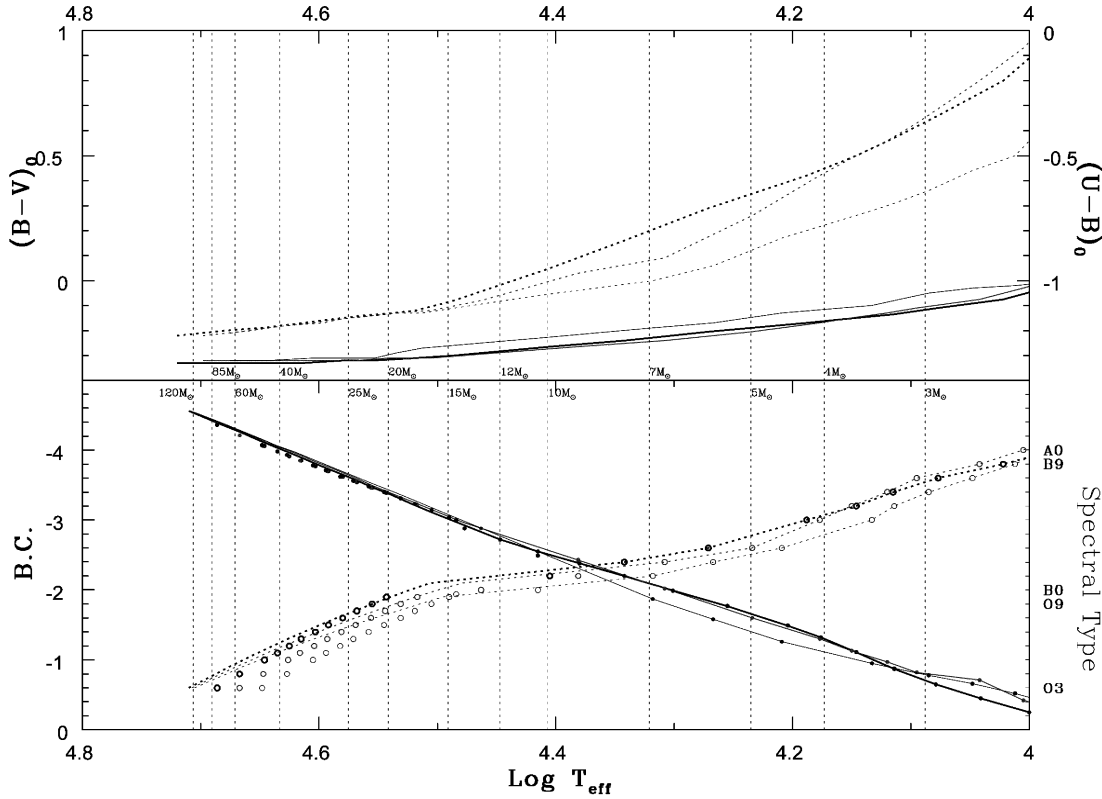
Fig. 1. Calibration relations for the conversion of observable to physical quantities. The dotted lines use the right hand axes and the solid lines use the left axes. Color transformations are from Schmidt-Kaler (1982); Bolometric Corrections (B.C.) and spectral type calibrations are and Malagnini et al. (1986) for the later spectral types merged smoothly with the calibrations for O-type stars of Vacca et al. (1996), lines, and Chlebowsky & Garmany (1991), dots. The effective temperatures of ZAMS stars of different masses have been drawn as vertical dotted lines.

of the measuring errors we can directly calculate the probability of obtaining a particular observation given a hypothesis. Then, Bayes' theorem is applied to obtain the probability of the hypothesis given the observation, once a suitable assumption about the *prior* probabilities of the hypothesis is made (see e.g. Kendall & Stuart 1977). The application of the Bayesian approach to the determination of the most probable age, initial mass, and reddening of the stars in 30 Dor given our UBV data is presented below.

2.2.1. Photometric solution

The first step is to produce a model of the observational errors. Because of error correlation effects it is simpler to work in a magnitude-magnitude space, as recently done by Tolstoy & Saha (1996), than to work in color-magnitude space. However, the additional complication of using colors is largely compensated by the fact that the CMS is conceptually simpler to interpret allowing us to better understand the data at the different stages of processing. Still, in order to model the errors it is convenient to start with the simpler magnitude-magnitude diagram generalized to three dimensions. In this space a measurement is represented by a vector $\mathbf{m}_*$ whose transpose is given by $\mathbf{m}_*^T = (V_*, B_*, U_*)$. The components of this vector are in-

dependent[2] and therefore the covariance matrix is diagonal. A measurement will be characterized by the pair $(\mathbf{m}_*, Q_\mathbf{m}^*)$, where $Q_\mathbf{m}^*$ is the *curvature matrix*, i.e. the inverse of the covariance matrix.

In the same space, a particular set of physical parameters for the star is represented, through the use of the calibrating relations (Fig. 1), by a vector $\mathbf{m}$. This value will be called the *true* magnitude of the star. The measurement process can be represented by a curvature matrix $Q_\mathbf{m}$. To solve the problem we have to assume that $Q_\mathbf{m} = Q_\mathbf{m}^*$.

Given that the observed value of a star's magnitude lies in a small neighborhood surrounding $\mathbf{m}_*$, let $p(\mathbf{m} \mid \mathbf{m}_*, Q_\mathbf{m}^*)$ be the conditional probability density that the *true* value of the star's magnitudes is $\mathbf{m}$. Using Bayes theorem with equal a-priori probabilities for the true stellar magnitudes it can be shown that

$$p(\mathbf{m} \mid \mathbf{m}_*, Q_\mathbf{m}^*) \propto p(\mathbf{m}_* \mid \mathbf{m}, Q_\mathbf{m}) \qquad (1)$$

which is just the statement that, for a given model for the measuring process, the probability of the *true* value given the measurement is proportional to the probability of the measurement given the true value. Assuming independent Gaussian errors we can then write

---

[2] Magnitude error correlation effects can be introduced by crowding but they are much reduced if colors are used instead, as can be seen in Fig. 5 of Paper I.
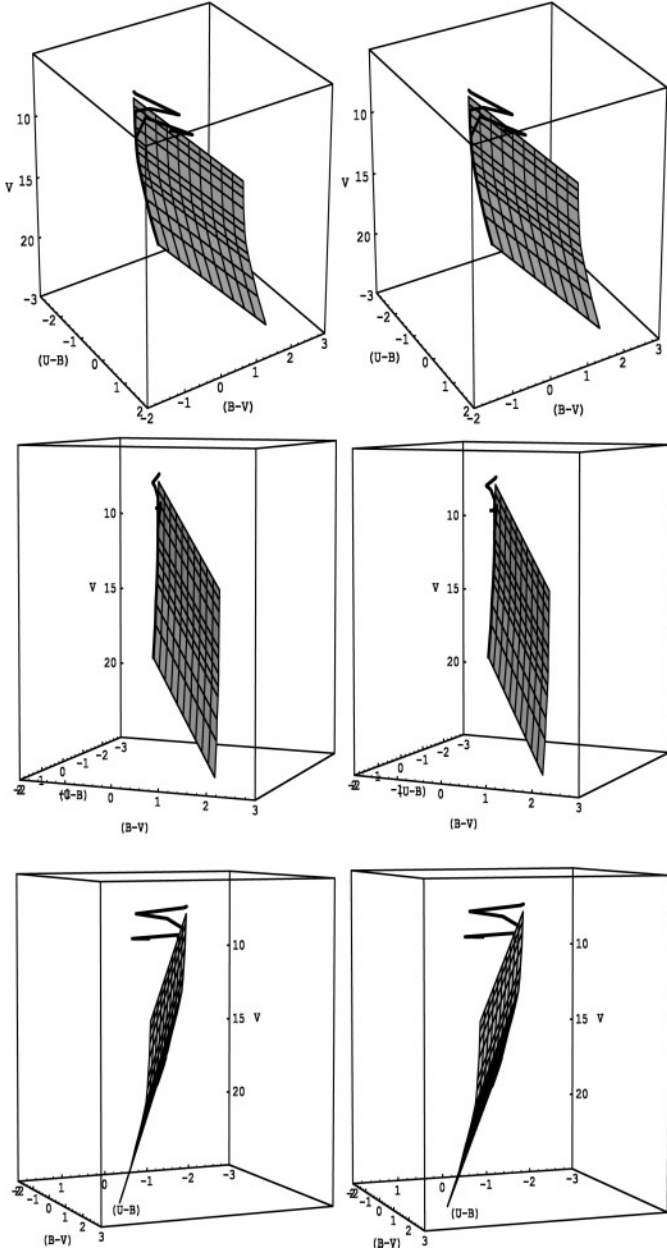
Fig. 2. The *theoretical surface*, described in the text, in the CM stereogram. The surface has been drawn for the 1 My isochrone with standard mass-loss. The reddening lines have been drawn for 120M$_\odot$, 85M$_\odot$, 60M$_\odot$, 40M$_\odot$, 25M$_\odot$, 20M$_\odot$, 15M$_\odot$, 12M$_\odot$, 10M$_\odot$, 7M$_\odot$, 5M$_\odot$, and 4M$_\odot$. A heavier line marks the 3 My isochrone. Another heavy line marks the 5 My isochrone which reaches only up to 40M$_\odot$! Notice in the upper viewpoint how evolution appears to get entangled with reddening. But the bottom perspective shows the degeneracy to be broken because evolution actually moves the star away from the reddening determined theoretical surface for a lower age isochrone.

$$p(\mathbf{m} \mid \mathbf{m}_*, Q_\mathbf{m}^*) \propto e^{-\frac{1}{2}[\mathbf{m}-\mathbf{m}_*]^T Q_\mathbf{m}[\mathbf{m}-\mathbf{m}_*]} \propto e^{-\frac{1}{2}\chi^2(\mathbf{m})}, \quad (2)$$

where $Q_\mathbf{m}^* = \mathrm{Diagonal}(\sigma_V^{-2}, \sigma_B^{-2}, \sigma_U^{-2})$. It can be shown that χ^2 is indeed distributed as the standard χ^2-distribution with 3 degrees of freedom (Brandt 1970). In case of non-Gaussian

errors we can keep the equation above changing to a different $\chi^2(\mathbf{m})$ function.

In the CMS space a measurement will be characterized by a vector $\mathbf{x}$ given by $\mathbf{x}^T = (\text{B-V}, \text{U-B}, \text{V})$. Since $\mathbf{x}$ is related to $\mathbf{m}$ by a unitary transformation, the probability density of $\mathbf{x}$ is given by

$$p(\mathbf{x}) = e^{-\frac{1}{2}[\mathbf{x}-\mathbf{x}_*]^T Q_\mathbf{x}[\mathbf{x}-\mathbf{x}_*]} \tag{3}$$

where $Q_\mathbf{x} = O^T Q_\mathbf{m} O, O\mathbf{x} = \mathbf{m}$. The price paid for working in color-magnitude space is that the covariance matrix $C_\mathbf{x} = Q_\mathbf{x}^{-1}$ is no longer diagonal.

The problem to be solved for each star is: given a measurement $(\mathbf{x}_*, Q_\mathbf{x}^*)$, find the most probable value for $\mathbf{x}$ subject to the condition that it should belong to the *theoretical surface.* Maximizing the probability is equivalent to finding the maximum of the likelihood function $L(\mathbf{x}) = \log\ p(\mathbf{x})$, or the minimum of $\chi^2(\mathbf{x}) = -2 \times L(\mathbf{x})$. Unless the matrix $Q_\mathbf{m}$ is singular (a situation that can not occur unless one or more of the measurement errors is equal to zero), the solution to the problem always exists. The reader can convince him/herself of this by considering χ^2 as a quadratic form, and realizing that there will always exist a value of χ^2 for which the ellipsoid thus defined touches the theoretical surface. For reasonably smooth theoretical surfaces the solution will be unique.

Let us parameterize the isochrone for time t with the initial mass M_i. Then, in the CMS it is represented by the equation $\mathbf{x} = \mathbf{x}_t(M_i)$. The theoretical surface is then represented by the equation

$$\mathbf{x} = \mathbf{x}_t(M_i) + \text{E(B-V)} * \mathbf{R}, \tag{4}$$

where $\mathbf{R}$ is the reddening vector $\mathbf{R} = (1, S, R_V)$, and E(B-V) is the color excess. Thus, for a given M_i and t the color excess which minimizes χ^2 is given by

$$\text{E(B-V)} = \frac{[\mathbf{x}_* - \mathbf{x}_t(M_i)]^T Q_\mathbf{x}^* \mathbf{R}}{\mathbf{R}^T Q_\mathbf{x}^* \mathbf{R}}. \tag{5}$$

The actual procedure used to find the most likely values of M_i, t, and E(B-V) for a star is as follow: first, a library of isochrones is prepared; each isochrone in the library consists of a tabulation of M_i, T_{eff}, and M_{bol}, together with the calibration relations which permits the calculation of the vector $\mathbf{x}_t(M_i)$, that is, magnitude and colors. Once the library has been set up the following procedure is carried out for each star:

1. from its observed magnitudes calculate the matrix $Q_\mathbf{x}^*$ and the vector $\mathbf{x}_*$;
2. for each isochrone indexed by its age, t, find the mass, M_i, and E(B-V) from Eq. (5), which minimizes the χ^2 implicitly defined in Eq. (2);
3. assign the probability defined by Eq. (3) to the solution determined in the previous step;
4. calculate average values and variances of the physical parameters over the whole set of isochrones using the probabilities as weights.

Although this is not the most computationally efficient method it avoids the convergence problems introduced by the complex topology of the theoretical surfaces at high masses.
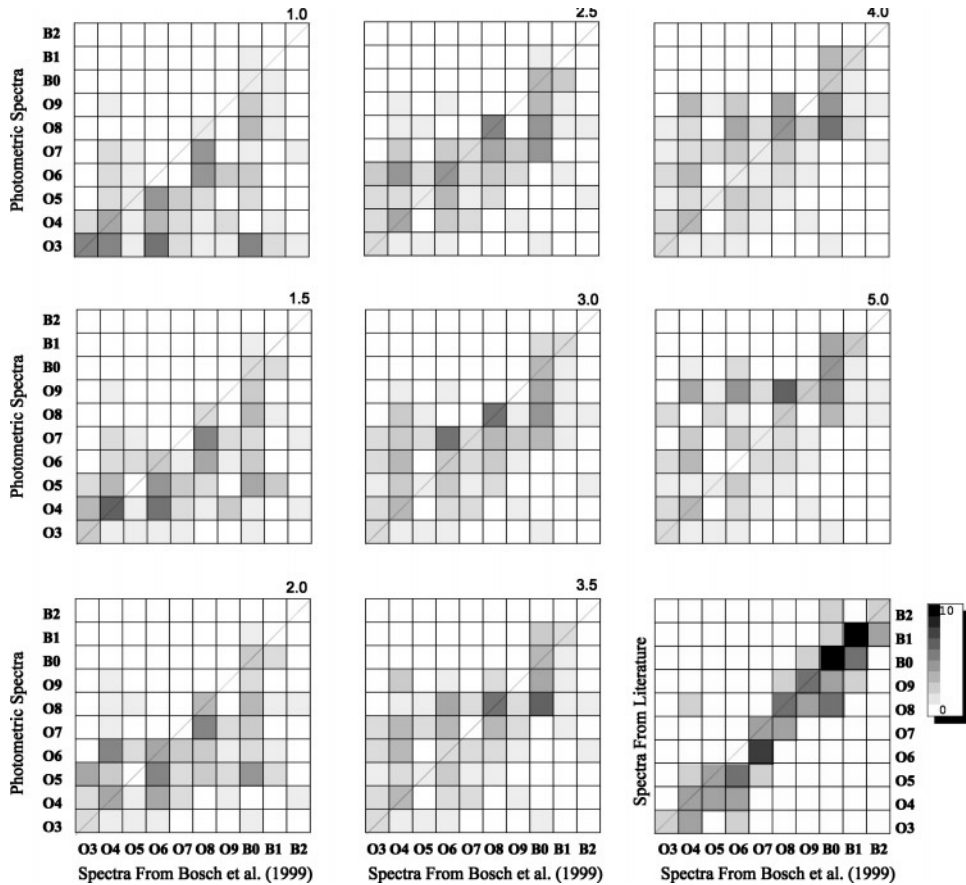
Fig. 3. Comparison of spectral types obtained photometrically as described in the text, with the "true" spectral types determined in Paper II. The comparison is done for eight libraries of isochrones (Z=0.008, twice standard mass-loss rates). The number in the upper right of each comparison indicates the age in My of the oldest isochrone employed; between 0 and the maximum age the isochrones are uniformly distributed. The plot in the lower right panel compares the spectroscopic types from Paper II to values from the literature and gives an indication of the uncertainties in the "true" spectral types (the literature types are mainly from Melnick 1985, Parker & Garmany 1993, and Walborn & Blades 1997). These diagrams show that the O3–O6 stars can be modeled with isochrones not older than 2.5My, but for the later classes it is necessary to include older isochrones.

2.2.2. Spectroscopic solution

Spectroscopic observations for 85 of the stars in the frame can be used to better constrain their physical parameters. To get a second solution as independent as possible from the photometric solution, we will disregard color information and use only spectral types and V magnitudes. The procedure is formally equivalent to the photometric one with a different χ^2 function.

The spectroscopic data can also be used to check the photometric solution. This is done by comparing the stellar types predicted photometrically with those obtained through spectroscopy. The photometric types depend on the star-formation history one assumes for the cluster. This is illustrated in Fig. 3, which compares our photometric spectral types with those measured spectroscopically. The correlation obtained when comparing spectroscopic types from different authors is shown for reference. The figure shows that the photometric method is able to predict spectral types with an accuracy of 3 subtypes approximately (0 to 3.0 My case). More importantly, this can be done without introducing a large bias towards later spectral types as is the case with the traditional method (e.g. Massey 1998).

An independent check of the method can be obtained by combining the spectroscopic solution with the photometric one. This is presented in the Appendix where a distance modulus of $(m - M)_0 = 18.45 \pm 0.15$ to the LMC is obtained, in excellent agreement with previous work (e.g. Gieren et al. 1998).

2.3. The HR diagram

Fig. 4 shows the HR diagrams determined with this method using the VGS effective temperature scale, the SchK effective temperature to color transformation, and the Geneva isochrones for standard (Schaerer et al. 1993) and twice standard (Meynet et al. 1994) mass-loss rates. The stars with spectroscopy are represented with open circles and the stars with photometry alone by small dots. The physical parameters of the stars have been determined with the Bayesian method using an uniformly populated library of isochrones from 0.1 My to 145 My.

Several points can be made from these diagrams. First, our transformation from observable to physical quantities is rather insensitive to the mass-loss rates assumed for the theoretical models. Second, the VGS calibration from colors to effective temperatures might introduce a spurious turn-off at approximately 1 My because its highest temperature is still below that of the isochrones. Third, there is a spurious concentration of data points at $\log T_{eff} \sim 4.2$ and $M_{bol} \sim -2$ which results from the photometric errors of stars with masses $M < 10 M_\odot$. Since the photometric errors are larger than the evolutionary change in colors for stars in this mass range, stars tend to cluster near the average of the isochrone library (0.1–145 My). The last point we wish to remark is that there is a group of stars that appear to have masses $M > 120 M_\odot$. This suggests that the upper mass limit of the IMF may be larger than $\sim 120 M_\odot$, although we cannot exclude that some of these stars may be massive binaries, or
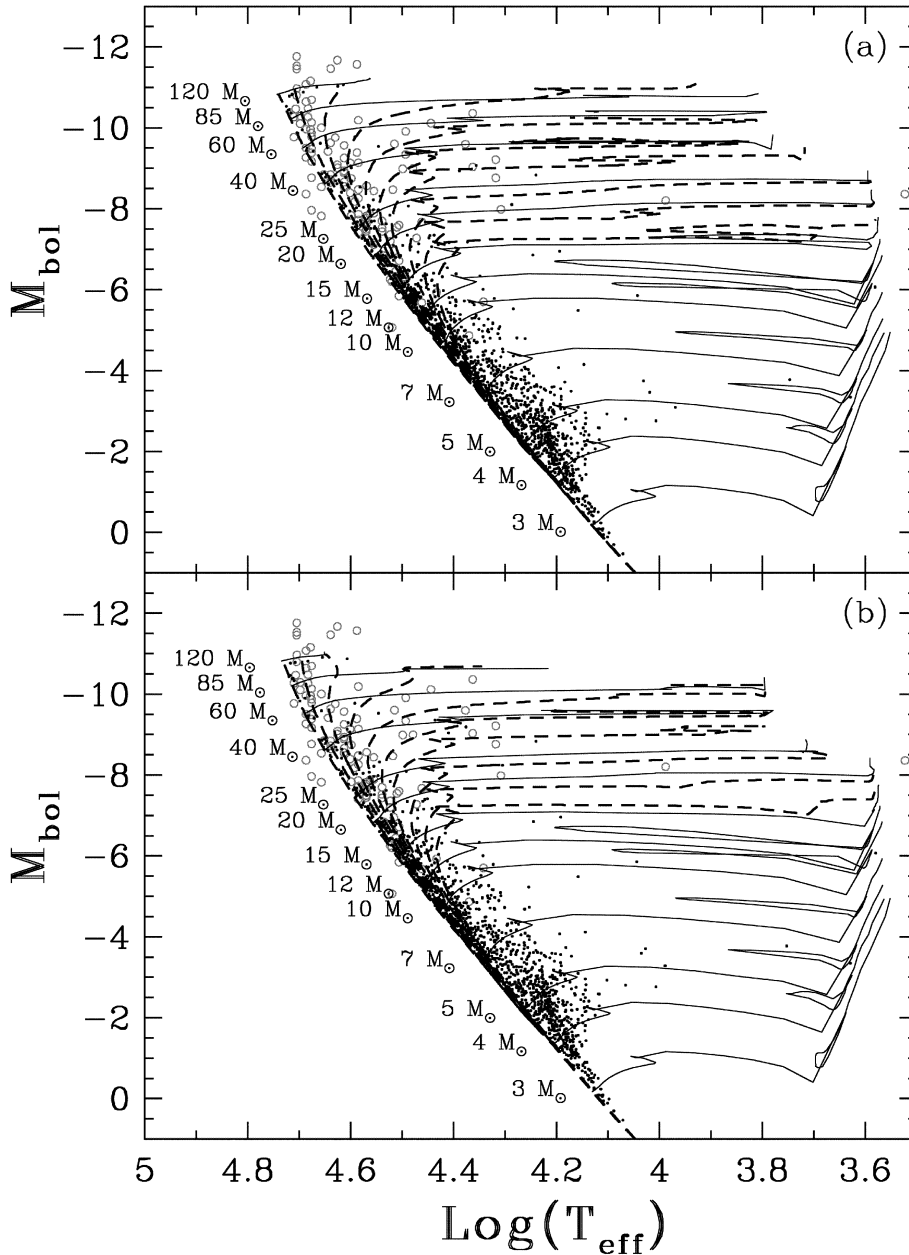
Fig. 4a and b. HR diagram of NGC 2070. The open circles represent stars with spectral types from Paper II. The dots show the positions of the stars from photometry alone. The solid lines show the Geneva tracks for Z=0.008 and the standard **a** and twice the standard **b** mass loss rates. The dashed lines plot isochrones of 0.1, 1, 2, 3, 4, 5, 6, 8, 10, and 12 My.

that physical effects such as mixing or rotation (not considered in the models) are affecting the mass determinations.

For the discussion it is important to summarize our results from the HR-diagram as follows: (1) while from photometry alone we cannot constrain the ages for the low mass and for some of the intermediate mass stars (for those with $M < 10 M_\odot$), we can still reliably determine their masses if we know their ages (e.g by assuming that they have the same formation history as the more massive stars in the cluster); (2) the rapid rate of evolution of the high mass stars, although not accurately known because of the uncertainties in their mass-loss rate, permits us to determine their ages, and thus, study the star-formation history of the cluster.

2.4. Systematic errors

A most delicate step in the determination of the IMF of a cluster is the determination and control of systematic effects. Once a set of stellar evolutionary models and a T_{eff}-color calibration has been chosen, the process is in principle straightforward: count the number of stars that fall in each (logarithmic) mass bin.

There are two main complications when applying this procedure to real data. The first is the well known problem of determining the incompleteness corrections. The second complication is due to the *magnitude-limit correction*: for a given absolute magnitude a star will have a different probability of being included in a magnitude-limited sample depending on the amount of reddening along its line of sight. For $A_V = 3.0$, even stars with absolute magnitudes as bright as $M_V = -2.5$ are affected

by this effect in a sample with magnitude limit $V_{lim} = 19.0$. This corresponds to a zero-age main sequence mass of approximately $15 M_\odot$.

2.4.1. The incompleteness correction

Artificial stars were created with a uniform distribution of magnitudes and colors over the range spanned by the real stars (omitting only the very reddest stars). These stars were then added to the original frames with the appropriate instrumental magnitudes calculated using the inverse of the instrumental equations determined in Paper I to create the catalogue of real stars. Each artificial star was then added at the appropriate location in each of the frames analyzed (remembering the small frame offsets). To avoid changing the crowding by too much the artificial stars were added a few at a time in many Monte Carlo experiments, such that less than $\sim 15\%$ of the total number of stars in the frames were added at a time. *Daophot II*'s `addstar` was used within the PC/LINUX IRAF environment to actually add the stars to the frames. The frames with the artificial stars were then reanalyzed from beginning to end in exactly the same way as the final data was. In doing this it was found that the recovery probability depended not only on the magnitude of the stars, but also on their colors. In addition, the the recovery probability depends locally on the surface density of stars[3]. More than 40 000 artificial stars were added to the frames in more than 200×3 experiments. A script was written to automate the process. Each experiment took approximately 14 minutes to run on a 200MHz Pentium Pro machine.

When calculating the IMF each of the real stars will contribute not one star, but a number equal to the inverse detection probability. This number depends on the position (or rather the local stellar surface density, ρ) of the star, its magnitude, V, and its color, (U-B). To determine it star-by-star we created a table (see Table 1) with the results of the MC experiments, and use a 3-dimensional cubic splines interpolation routine (Press et al. 1994) to determine, for a given $(\rho, V, (U-B))$, its detection probability. For easy reference we include in Table 1 the actual number of stars added, Nadd, the number of stars recovered, Nrec, and the detection probability, p.

The maximum density for which we can determine reliable incompleteness corrections depends on the number of Monte-Carlo experiments one can perform in a reasonable amount of time. The 600 experiments performed here took approximately 140 CPU hours, and, for $V < 19.5$, permit us to correct the data up to $\log \rho \approx 3.3$, where, ρ, the local stellar surface density is measured in stars per arcmin^2 (for $r > 15''$ the surface density is smaller than this for all but one star, see Fig. 5).

Fig. 5 shows scatter plots of the data as a function of V magnitude, radial distance to the cluster center, and local stellar

---

[3] A code was written to determine the local stellar density around each of the artificial stars. This program takes each artificial star position and determines approximately the largest square that contains it and none of the real stars. The inverse of this area is used as an approximate measure of the local stellar density. The algorithm to do this is similar to that in the tree-code of Barnes & Hut (1986).
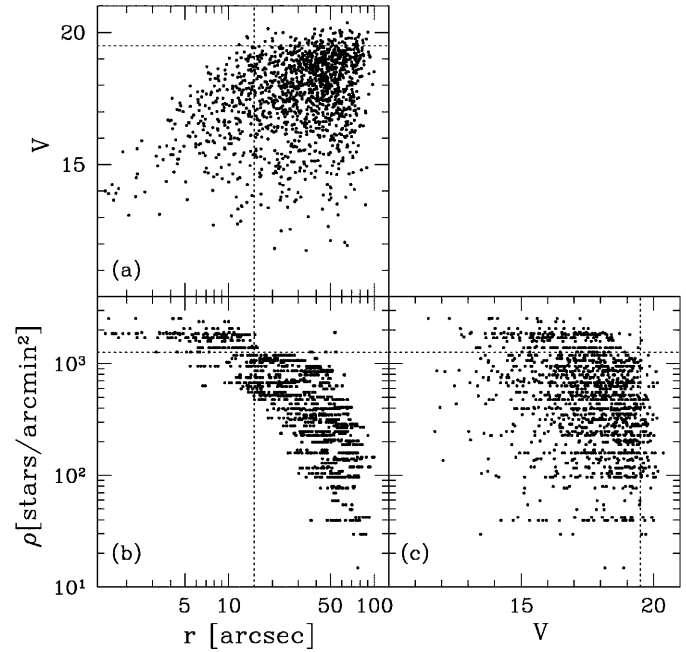

Fig. 5a–c. a V magnitudes as a function of distance to the cluster center for the whole sample of stars. The upper envelope of the cloud of points defines the magnitude limit of the photometry. **b** Log of the stellar density as a function of distance to the cluster center. **c** Same as **a** but as a function of local stellar density (with axes interchanged).

density. The Monte-Carlo experiments show that the apparent boundaries defined by the sharp decrease in the number density of points at high stellar densities and small radial distances are due to incompleteness effects and have no physical significance. These figures can then be used to construct "fair" samples for the study of the IMF defined as regions in these diagrams where the incompleteness corrections are well established.

We have thus constructed two samples: an *outer* sample defined by $r > 15''$, which is "fair" down to $V \approx 19.5$, and an *inner* sample defined to correspond to the outermost sample of the HST study of Hunter et al. (1995, 1996), and which is "fair" down to $V \approx 17 (r > 4.6'')$.

2.4.2. The magnitude-limit correction

Once the incompleteness correction has been determined it becomes necessary to apply the *magnitude-limit correction*. This correction can be understood by tracing the steps for the conversion from physical parameters to observed magnitude and colors. Consider a B3 zero age main sequence star, which according to SchK has an absolute magnitude of $M_V \approx -1.1$ and a mass of $M \approx 7.6 M_\odot$. At zero reddening this star would have an apparent magnitude $V = 17.40$, well within the magnitude limit of the catalogue in Paper I ($V_{lim} = 19.2$). Nevertheless, this star would not be included in a photometry with a cut-off at this magnitude limit if $A_V \gtrsim 1.8$.

Correcting for incompleteness alone does a proper job for all stars whose absolute magnitude is brighter than $V_{lim} - (m - M)_0 - A_V^{max}$, where A_V^{max} is the maximum total extinction

Table 1. Results of artificial stars experiments. The number in parenthesis below the density range denotes the average density for all the stars in that range; Nadd is the number of stars added; Nrec is the number of stars recovered; p is the detection probability. The total number of added stars in the table is 38646, which together with the 1500 stars used to study systematic errors in Paper I make a total of 40 146.

| $\log \rho$ [stars/arcmin^2]	V	$-1.5 < (U-B) < -0.5$			$-0.5 < (U-B) < 0.0$			$0.0 < (U-B) < 0.5$		
		Nadd	Nrec	p	Nadd	Nrec	p	Nadd	Nrec	p
$\log \rho > 3.2$	$V < 15.0$	62	59	0.952	48	42	0.875	29	28	0.966
(3.23)	$15.0 < V < 16.0$	56	52	0.929	47	36	0.766	38	29	0.763
	$16.0 < V < 17.0$	85	71	0.835	52	41	0.788	32	21	0.656
	$17.0 < V < 18.0$	147	70	0.476	144	60	0.417	113	38	0.336
	$18.0 < V < 18.5$	69	23	0.333	79	21	0.266	66	13	0.197
	$18.5 < V < 19.0$	73	10	0.137	62	12	0.194	64	3	0.047
	$19.0 < V < 19.5$	79	5	0.063	76	4	0.053	72	3	0.041
	$19.5 < V < 20.0$	177	0	—	189	0	—	215	0	—
$3.0 < \log \rho < 3.2$	$V < 15.0$	60	54	0.900	49	40	0.816	42	37	0.881
(3.07)	$15.0 < V < 16.0$	79	74	0.937	51	43	0.843	40	30	0.750
	$16.0 < V < 17.0$	80	70	0.875	49	41	0.837	41	27	0.659
	$17.0 < V < 18.0$	231	164	0.710	243	151	0.621	187	102	0.545
	$18.0 < V < 18.5$	98	49	0.500	101	59	0.584	96	34	0.354
	$18.5 < V < 19.0$	96	34	0.354	103	34	0.330	102	24	0.235
	$19.0 < V < 19.5$	98	12	0.122	93	19	0.204	97	10	0.103
	$19.5 < V < 20.0$	211	11	0.052	230	4	0.017	231	0	—
$2.8 < \log \rho < 3.0$	$V < 15.0$	133	126	0.947	118	115	0.975	105	100	0.952
(2.90)	$15.0 < V < 16.0$	118	113	0.958	108	101	0.935	104	97	0.933
	$16.0 < V < 17.0$	161	153	0.950	145	128	0.883	122	110	0.902
	$17.0 < V < 18.0$	548	477	0.870	566	466	0.823	498	384	0.771
	$18.0 < V < 18.5$	271	217	0.801	240	189	0.787	238	153	0.643
	$18.5 < V < 19.0$	264	175	0.663	281	175	0.623	248	103	0.415
	$19.0 < V < 19.5$	231	112	0.485	276	109	0.395	214	58	0.271
	$19.5 < V < 20.0$	584	44	0.075	580	45	0.078	607	13	0.021
$2.6 < \log \rho < 2.8$	$V < 15.0$	75	70	0.933	62	60	0.968	55	52	0.945
(2.71)	$15.0 < V < 16.0$	66	58	0.879	45	44	0.978	47	47	1.000
	$16.0 < V < 17.0$	67	58	0.866	82	79	0.963	57	51	0.895
	$17.0 < V < 18.0$	271	238	0.878	247	221	0.895	212	179	0.844
	$18.0 < V < 18.5$	129	107	0.829	139	110	0.791	127	90	0.709
	$18.5 < V < 19.0$	128	91	0.711	158	105	0.665	122	47	0.385
	$19.0 < V < 19.5$	125	65	0.520	132	49	0.371	109	18	0.165
	$19.5 < V < 20.0$	284	18	0.063	289	14	0.048	295	8	0.027
$2.2 < \log \rho < 2.6$	$V < 15.0$	243	237	0.975	212	209	0.986	270	263	0.974
(2.41)	$15.0 < V < 16.0$	184	177	0.962	198	197	0.995	202	198	0.98
	$16.0 < V < 17.0$	238	230	0.966	220	212	0.964	206	194	0.942
	$17.0 < V < 18.0$	1086	1043	0.960	1129	1064	0.942	1034	973	0.941
	$18.0 < V < 18.5$	556	527	0.948	611	567	0.928	530	471	0.889
	$18.5 < V < 19.0$	529	476	0.900	601	489	0.814	500	339	0.678
	$19.0 < V < 19.5$	504	370	0.734	527	321	0.609	512	219	0.428
	$19.5 < V < 20.0$	1321	156	0.118	1405	125	0.089	1418	68	0.048
$\log \rho < 2.2$	$V < 15.0$	160	159	0.994	154	153	0.994	146	145	0.993
(2.05)	$15.0 < V < 16.0$	131	130	0.992	114	112	0.982	104	102	0.981
	$16.0 < V < 17.0$	137	136	0.993	123	121	0.984	121	119	0.983
	$17.0 < V < 18.0$	732	713	0.974	713	696	0.976	705	672	0.953
	$18.0 < V < 18.5$	370	357	0.965	388	371	0.956	311	283	0.910
	$18.5 < V < 19.0$	390	366	0.938	388	332	0.856	334	235	0.704
	$19.0 < V < 19.5$	389	286	0.735	381	251	0.659	349	164	0.470
	$19.5 < V < 20.0$	982	157	0.160	947	104	0.110	920	47	0.051
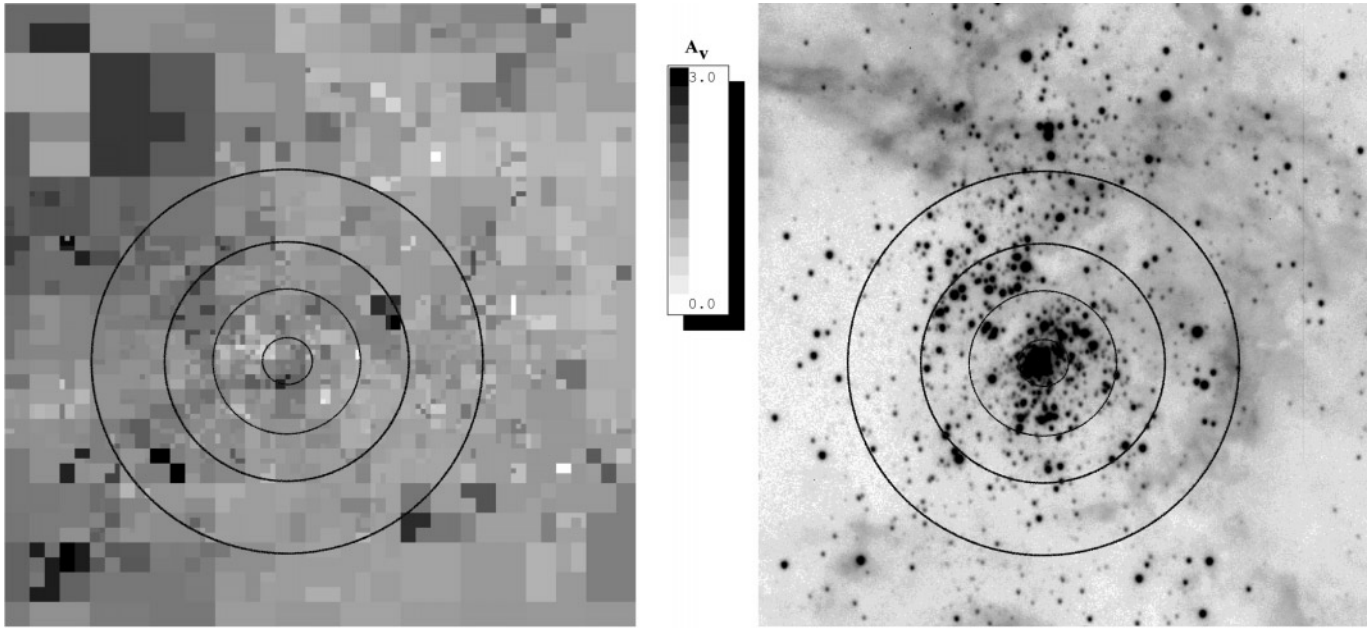
Fig. 6. The probability distribution of visual absorption Av. The top panel shows that the extinction distributions of high mass and low mass stars are virtually identical. The bottom panel separates the sample using the radial distance to the cluster center. There is a clear trend of larger extinction towards the cluster center (which can not be the result of systematic errors, as discussed in Paper I). Only stars brighter than V=16.2 have been included in the bottom panel to ensure a fair sample.

for the stars in the cluster. Fig. 6 shows that for 30 Doradus this value is given by $A_V^{max} \approx 3.0$. Thus, the catalogue can be used with incompleteness correction alone only down to $V = 16.20$, which corresponds to $M_V = -2.3$, or $13 M_\odot$. Parker & Garmany's (1993) catalogue is complete to $V = 18.0$, which would translate to $M \approx 20 M_\odot$.

Stars with $M_V = -1.1$ and $A_V \lesssim 1.8$ will be included in the catalogue with a probability given by the incompleteness correction for the appropriate apparent magnitude, color, and position in the frame. *All those stars with $A_V \gtrsim 1.8$ will be lost.* Thus, for each star of this absolute magnitude detected a further correction should be applied: the star contribution to the appropriate mass bin should be divided by the probability of inclusion, i.e. the fraction of these stars with $A_V \lesssim 1.8$. This fraction can be calculated assuming that the probability distribution A_V is independent of absolute magnitude. The probability of inclusion is then given by the area under the curve in Fig. 6 between $A_V = 0$, and $A_V = V_{lim} - V$.

This reddening induced problem has already been recognized in a few recent studies of deeply embedded clusters. The complications introduced by reddening become most severe in the study of these clusters, as recognized in the recent infrared work of Meyer (1996). Nevertheless, in order to apply the magnitude-limit correction it is necessary that A_V^{max} be well defined. Fig. 6 shows that this is indeed the case for NGC2070. For the extremely embedded clusters the situation is not as fortunate, and a limit for A_V^{max} is not evident in the data (e.g. Fig. 6 of Carpenter et al. 1997). In this case it becomes necessary to select a subsample of the data imposing an upper limit for A_V in what is called an A_V-limited sample (Meyer 1996).

For the correction to work we should be able to define a meaningful reddening distribution. First, if present, systematic differences in reddening for stars of different mass should be considered. In Fig. 6a the stars have been divided into two sub-samples of different masses. Using the χ^2 test we find that the hypothesis that the two samples have been drawn from the same distribution can only be rejected at the 10% confidence level. It is then appropriate to use the same distribution of reddening for stars of different masses.

A different conclusion is reached after examining Fig. 6b, where the sample has been subdivided according to the distance of the stars to the cluster center. In this case a χ^2 test shows that the hypothesis that the two samples have been drawn from the same parent distribution can be rejected at the 99.5% confidence level. This is the photometric counterpart to the conclusion reached in Paper I, based on the spectroscopy and photometry, that there is a reddening component associated to the cluster itself, and that the average reddening due to this component increases towards the center (Fig. 5 of Paper I shows that this can not be a systematic effect due to a higher probability of blending near the center: no systematic trends with radius were uncovered by the MC experiments reported in that work).

Fig. 7 stresses the importance in determining the reddening for each star individually. It shows a reddening map, together with a reference B image. The map was created with a recursive tree algorithm specially designed to preserve the high resolution in higher stellar density areas. We can appreciate that together with the high spatial variability, there are some clear large scale trends, the most noteworthy being an east west gradient, an area of increased reddening towards the north-east, and a zone of
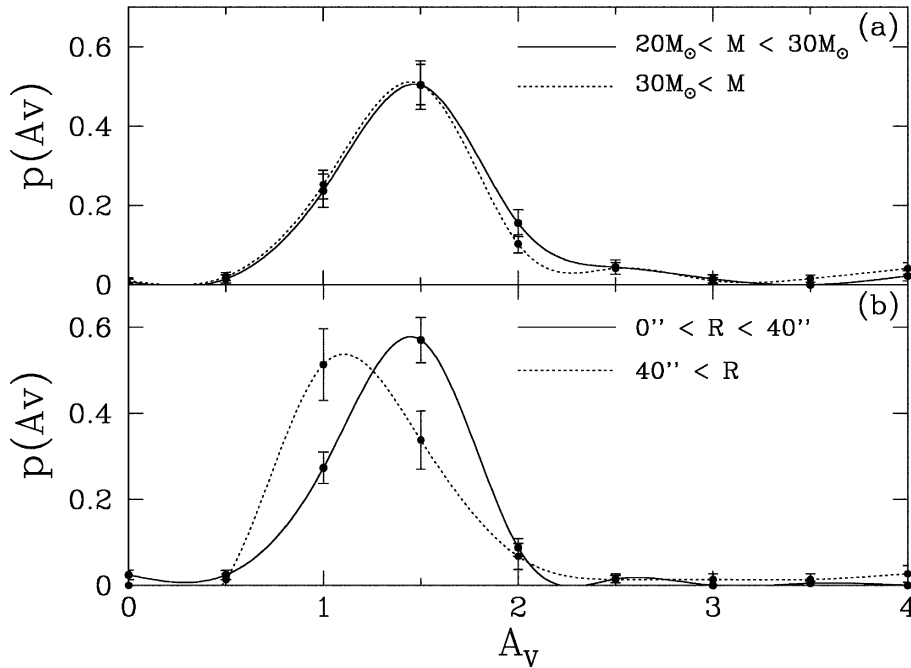
Fig. 7a and b. Reddening map of 30 Doradus calculated with an adaptive algorithm to preserve spatial resolution. The circles are centered in R136 with radii of $5''$, $15''$, $25''$, and $40''$. The image is a copy of the B frame employed for the photometry. The reddening scale goes from Av=0 to Av=3.0, calculated assuming Rv=3.05. North is up and east to the left; size is $133''$ or $\sim$30 pc.

large reddening variation with an above average mean near the cluster center[4].

3. Results and discussion

3.1. The star-formation history of 30 Doradus

The star-formation history presented by Massey & Hunter (1998a, 1998b) asserts that the massive stars formed last, in accordance with the *sequential* picture proposed by Herbig (1962). The large number of O3 stars observed by HST is thus explained as an age effect: these extremely massive stars, which do not last for more than 1My, were the last to form quenching any further star formation in the center of the cluster. An alternative picture of star formation, which has been called *contemporaneous* by Stahler (1985), proposes that the star formation rates of stars of different masses is not a function of time: at all masses the probability of formation, although fluctuating, is approximately constant since the beginning of the star formation event. When averaged over the lifetime of the cluster we find a higher average star formation rate for the less massive stars, precisely the information contained in the IMF. In contrast to the sequential star formation scenario, but also stochastically, the most massive stars can appear at any time during the lifetime of the cluster with equal probability. According to Elmegreen (1997) the presence or absence of high mass stars depends on the total

number of stars formed according to a *stochastic sampling* of an universal IMF.

Fig. 8 shows the star-formation history of 30 Doradus determined using the ages and masses derived from the Bayesian method and equally likely isochrones up to 15My. The upper curve on the top panel gives the main sequence lifetime as a function of mass (defined as that point in the evolution when the surface fraction of Hydrogen falls below 40%.) The lower curve gives 1σ errors in the estimated ages[5]. For $M > 40M_\odot$ the photometric solution gives approximately the same star-formation history as the spectroscopic one. Below this limit there is a tendency for the photometric solution to track the mean isochrone of the library. Thus we have used both the spectroscopic and the photometric solutions to draw the high mass histogram shown in the lower panel. For the low mass histograms we have used only stars with spectroscopy. Three unresolved peaks in the star-formation rate are clearly seen in this figure: a *young* peak at $0 < t < 1.5My$, a *middle-age* peak at $1.5My < t < 3.5My$, and an *old* peak at $4My < t < 6My$. The weakness of the young peak in the lower mass bin is an artifact introduced by the incompleteness of the spectroscopy for these stars.

Fig. 9 shows the spatial distribution of the stars in the three age groups. The region within $15''$ is populated almost exclusively by young stars (green dots) while the other two groups tend to avoid this region. Even outside the central region the young stars appear to be more clustered than the middle-age stars (yellow dots), which in turn appear to be significantly more clustered than the old stars (red dots). Also shown in Fig. 9 are the O3If/WN and the WR stars which appear mostly within

---

[4] This way of presenting the reddening data emphasizes the spatial variations while optimizing spatial resolution. Showing these variations is what we wanted to accomplish with it. The average excess reddening towards the center is only barely discernible in this picture because: (1) the effect is small (0.5 mags); and (2), the reddening of a few highly reddened stars near the outskirts of the clusters dominate a much larger area, giving them a much larger weight in our perception.

[5] The absence of stars more massive than $100M_\odot$ and younger than 0.5My is an artifact of using a set of evolutionary tracks with an upper mass limit apparently below the highest masses present in the cluster (see discussion on upper mass limit below).
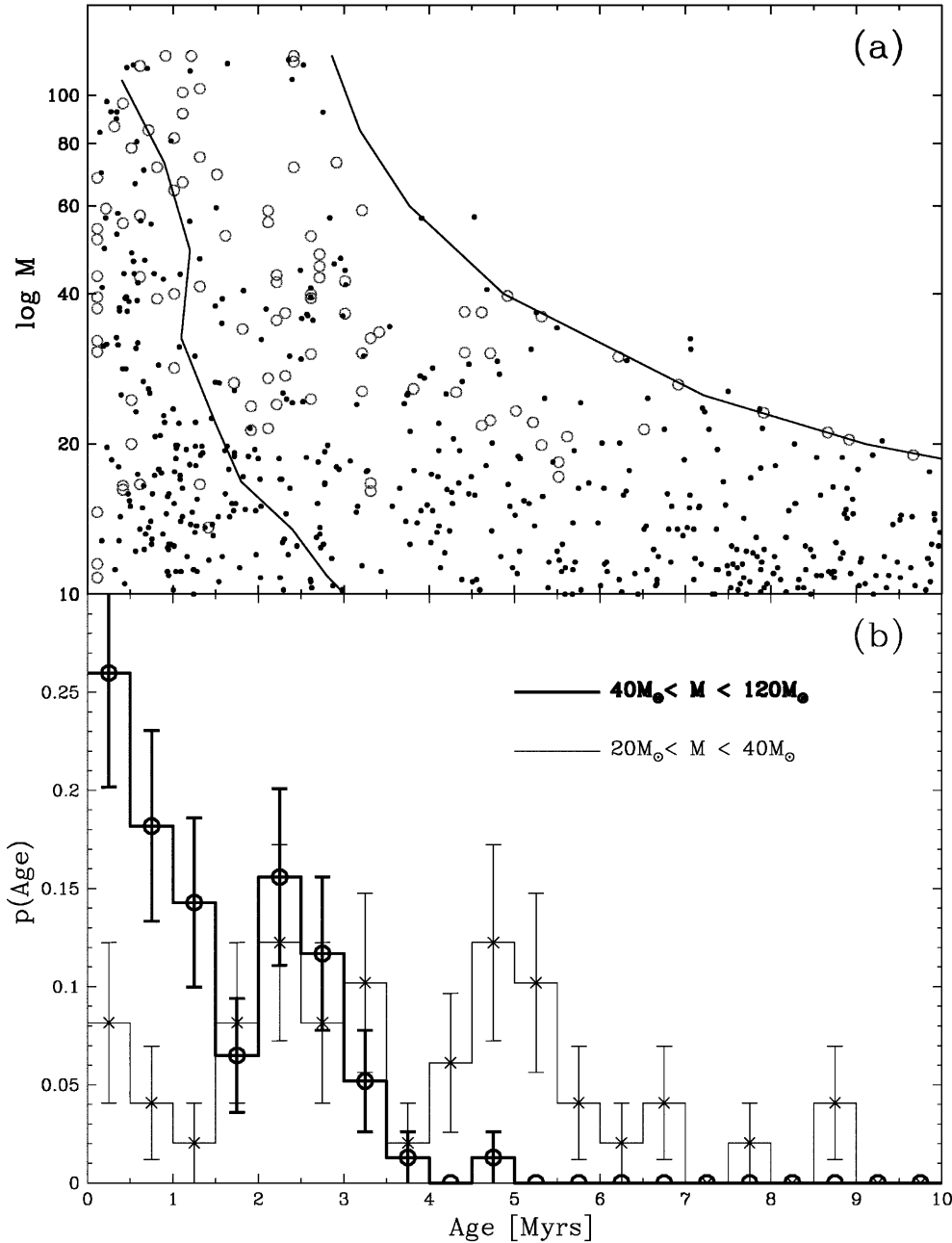
Fig. 8. a Star-formation history as a function of mass. The curve that envelopes the data shows the main sequence lifetime as a function of mass. The lower curve gives an estimate of the 1σ errors in the ages, determined using a weighted average of the square deviations from the determined mean ages. Solid dots represent stars placed with photometry alone; open circles represent stars placed with spectroscopy and their V magnitudes. Above $40 M_\odot$ both sets of points reveal the same history. **b** Histograms of ages for the stars with $r > 5''$: the heavy line was drawn using spectroscopic solution if available, and photometric solution otherwise. The thin line was drawn using spectroscopic data exclusively. Three different episodes of star formation appear to be revealed by the data.

$r < 15''$, with a few of the WR stars associated with subgroups located at $r > 40''$ (Brandl et al. 1996, coined the term "ring-like structure" to refer to the spatial distribution of these stars near the core). Two of the four O3If/WN stars are associated with the middle-age peak, but both are closer to the center than typical for that age group. The WR stars, supposed to have ages between 3My and 7My, would be associated with the old peak. They also appear spatially segregated from the rest of the stars in this age group.

The star-formation history of 30 Doradus appears to be dominated by three distinct bursts of increasing strengths which took place approximately 5My, 2.5My, and $\lesssim 1.5$My ago. The fact that the central parts of the cluster are populated almost exclusively by young stars, while both older and younger stars populate the periphery provides evidence that star formation propagated inwards. This appears to be contradicted by the distribution of WR stars which, being "old", are centrally concentrated. Note, however, that de Koter et al. (1997) have shown that several WR stars in the core of the cluster may, in fact, be very young. In that case their location near the center would be consistent with that of the rest of the young massive stars.

Working over a much wider area, Walborn & Blades (1997) identified five age groups in 30 Dor, three of which are similar to the ones identified here. Of particular interest are the 5My stars which appear to be uniformly spread over the face of the nebula supporting the idea that star formation propagated inwards in the cluster.
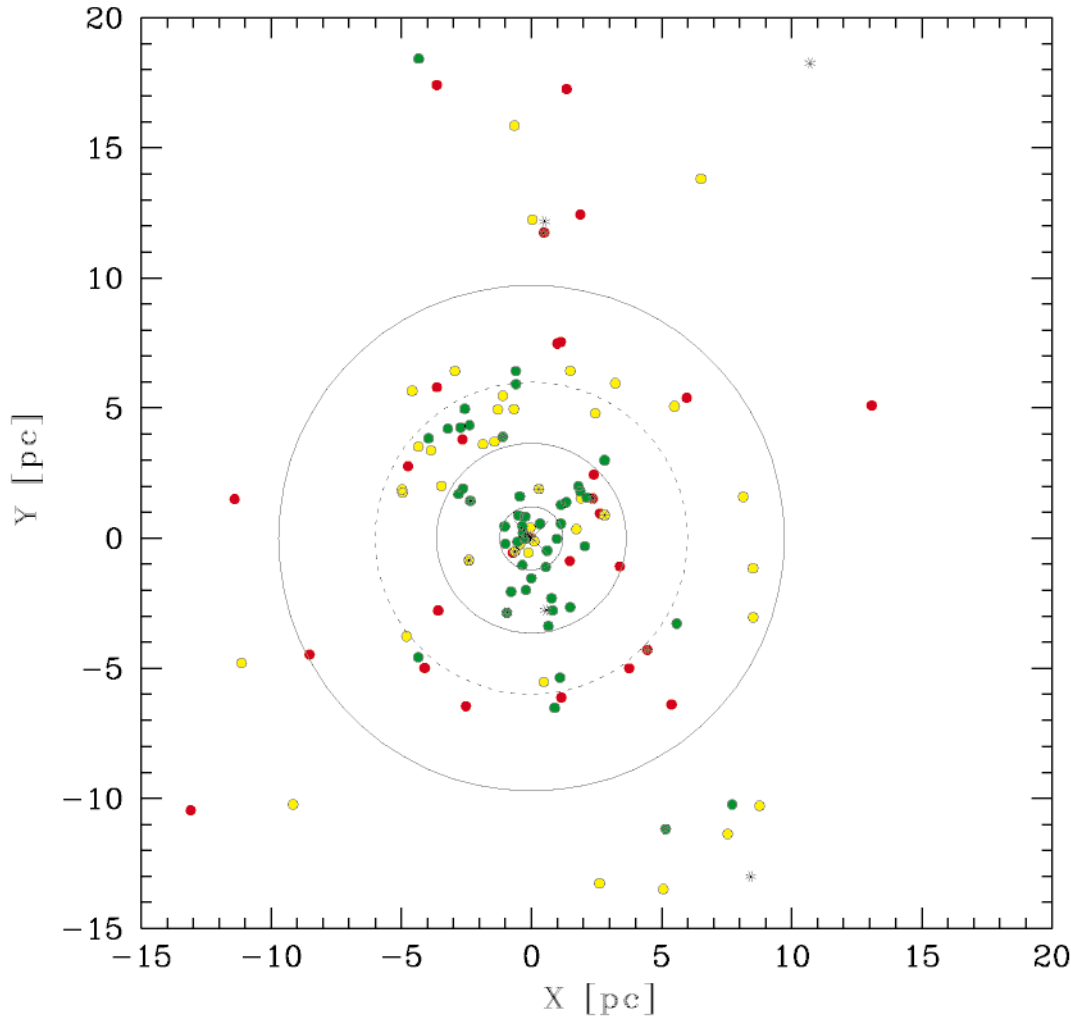
Fig. 9. Spatial distribution of stars with $M > 20M_\odot$ as a function of age. The color codes the position of the stars in the three episodes of star formation identified in Fig. 8: green for young peak, yellow for the middle-age peak, and red for the old peak. The O3If stars are the color dots with a superposed asterisk. The WR stars are plotted using an asterisk.

Brandl et al. (1996) combined near-infrared adaptive optics observations together with HST observations to study the star-formation history and IMF of a region $12''$ by $12''$ at a distance of $4''$ from the cluster center. In their Fig. 13, which is the equivalent of this paper's Fig. 8b, we can see three peaks of increasing intensity, separated by approximately 2.5My. Their three peaks are approximately 1My older than the ones derived in this work, a fact that might be attributable to the known problems with the HST photometry discussed in Paper I.

Our observations suggest that the formation of massive starburst clusters, such as 30 Dor, is more complex than the relatively simple *stochastic sampling* picture presented by Elmegreen (1997). While the model correctly predicts the IMF slope and the relation between stellar-mass and age we observe, it does not consider the effects of dynamical evolution and age clustering discussed above.

The fact that star formation appears to be synchronized over very large distances is puzzling and needs to be investigated

further by extending the present work over the whole face of the 30 Doradus superassociation.

3.2. Initial mass function of 30 Doradus

It is customary to define the IMF of a cluster as the number of stars per unit mass interval. The implicit assumption is that all the stars in the cluster are coeval i.e. that the age spread of the stars, Δt, is much smaller than the age of the cluster, τ_{cl}, $\Delta t << \tau_{cl}$. The IMF of coeval clusters can only be determined for stars less massive than the maximum mass still present in the cluster and more massive than the *pre-main-sequence* (PMS) cut-off: the minimum mass a star can have so that it has reached the main-sequence in the time available since the start of the starburst scenario. Thus, if $\tau_{MS}(M)$ is the main sequence lifetime for a star of mass M, the IMF can be derived up to a mass M which satisfies $\tau_{MS}(M) = \tau_{cl}$.

Since Δt cannot be arbitrarily small, for very young clusters such as 30 Doradus, $\Delta t \sim \tau_{cl}$, so the determination of the IMF is
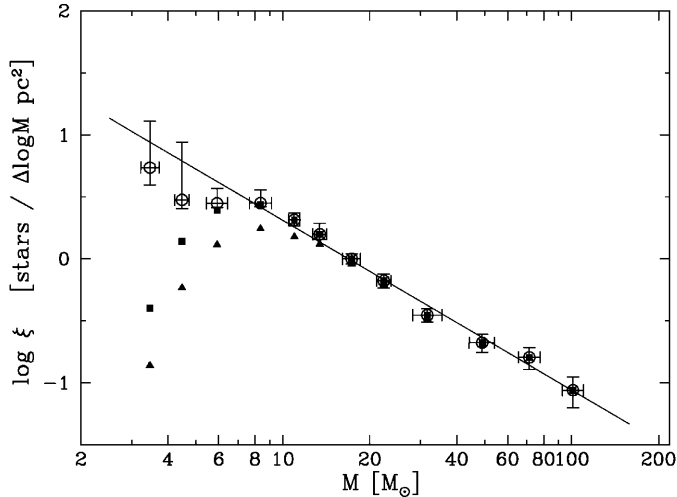
Fig. 10. The IMF of 30 Doradus for the sample of stars with $r > 15''$, calculated assuming equally likely isochrones below 3My. The line is a least squares fit to the data which gives $dN \propto M^{-2.37 \pm 0.08} dM$. The error bars consider counting statistics together with the errors in the incompleteness and magnitude-limit corrections.

Table 2. Initial Mass Functions

Radius[a] $''$	Mass $M_\odot$	$\log \xi$[b] $(\Delta \log M)^{-1} pc^{-2}$	$\sigma^+_{\log \xi}$	$\sigma^-_{\log \xi}$
15–75	85–119	−1.06	0.11	0.14
	60–85	−0.80	0.08	0.10
	40–60	−0.68	0.07	0.08
	25–40	−0.45	0.05	0.06
	20–25	−0.18	0.05	0.06
	15–20	−0.00	0.04	0.04
	12–15	0.20	0.09	0.04
	10–12	0.31	0.05	0.05
	7–10	0.45	0.11	0.03
	5–7	0.45	0.12	0.03
	4–5	0.47	0.47	0.07
	3–4	0.74	0.37	0.14
4.6–19.2	85–119	−0.07	0.13	0.19
	60–85	0.07	0.12	0.16
	40–60	0.17	0.11	0.13
	25–40	0.58	0.07	0.07
	20–25	0.66	0.10	0.10
	15–20	0.92	0.06	0.07
	12–15	0.97	0.08	0.09
	10–12	1.24	0.14	0.16
	7–10	0.90	0.25	0.41

[a] These are non-circular boundaries and the outer radii are effective in the sense of areas. The outer boundary of the outer sample is the square boundary of the NTT frame. For the inner sample the outer boundary is defined by the rectangular frame of the HST PC as defined in the text.

[b] For the $15''$–$75''$ region the best fit has $\log \xi_0 = 1.68 \pm 0.11$ and $\Gamma = 1.37 \pm 0.08$. The inner $4.6''$–$19.2''$ region, including the H96 data, is best fitted with $\log \xi_0 = 2.29 \pm 0.05$ and $\Gamma = 1.17 \pm 0.05$.

more complicated than just counting stars in different mass bins. The present day star counts are the integration in time of the star-formation rate, so, when dealing with non-coeval populations, it is appropriate to report an average *star-formation rate* as a function of mass rather than counts as a function of mass.

In order to compute this rate, the counts must be normalized by Δt for stars with masses smaller than those given by $\tau_{MS}(M) = \Delta t + \tau_{cl}$, and by the fraction of their main sequence lifetime spent in the star-formation episode for all other masses. If the star-formation episode continues until now, as is probably the case for 30 Doradus, this fraction is 100% and the normalization is simply $\tau_{MS}(M)$. Fig. 8 shows the star-formation history of 30 Dor as a function of mass. The bulk of the stars appear to have formed three bursts of strength increasing with time, and with the most massive starts preferentially formed in the most recent burst. Thus, the simple prescription of dividing the counts by a time interval which is only a function of stellar mass is incorrect. However, since all previous determinations of the IMF of 30 Dor report star counts as a function of mass and not the star-formation rate as a function of mass (Parker & Garmany 1993; Hunter et al. 1995; Hunter et al. 1996; Massey & Hunter 1998a, 1998b), we will continue the tradition in this paper keeping in mind that the IMF thus determined may not contain all the relevant physical information available in the data. For that it is indispensable to study Fig. 8.

The IMF determined in the outer and inner regions of the cluster, using Maeder's high mass-loss models for a metallicity of Z=0.008, together with the VGS effective temperature calibration is given in Table 2 and plotted in Figs. 10 and 11. There are three sets of points in these plots corresponding to the uncorrected counts, the counts corrected only for incompleteness, and the counts corrected for incompleteness and magnitude-limit effect. Between $3M_\odot$ and $120M_\odot$, the data are very well represented by a *single* power law of Salpeter slope.

3.2.1. Comparison with previous work

No single previous analysis of 30 Doradus, either from the ground or space, has the large coverage in mass that we present here and we are thus forced to compare our work with a combination of several published investigations.

For the outermost regions there is no correct space or ground-based determinations to compare our results with. The finding by Parker & Garmany (1993) of an IMF which is not well represented by a power law in any mass range is a result of their not recognizing the need to apply a magnitude-limit correction. Thus, our work is the only one available in this radial distance range. We can see in Fig. 10 that for $r > 15''$ the IMF is indistinguishable from Salpeter, with a slope $\Gamma = -1.37 \pm 0.05$ between $3M_\odot$ and $120M_\odot$.

For the inner region of the cluster we can compare with the HST observations of Hunter et al. (1995; H95) and Hunter et al. (1996; H96). Their outermost area extends from $4.6''$ out to the boundaries of the HST PC field. We have used their published list of coordinates to determine the transformation between our system and theirs and thus count stars in exactly the same region. This procedure is important due to the highly fluctuating stellar density distribution which would render a comparison based on counts between effective radii useless. H95 give $\Gamma = -1.17 \pm$
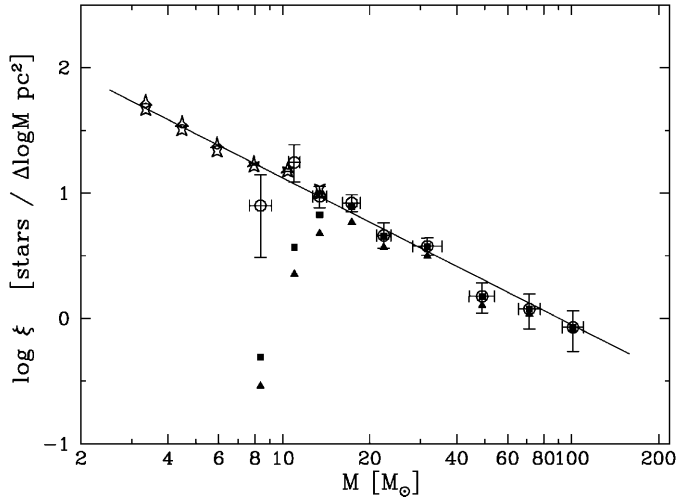
Fig. 11. The IMF of 30 Doradus for the region in common with the HST work of Hunter et al. (1995, 1996). The symbols are as in Fig. 10 with the addition of Hunter's IMF represented by the stars: 3 points H95, 4 points H96. The solid line is the best fit to this paper's data together with H96 which gives $dN \propto M^{-2.17\pm0.05}dM$. Error bars as in previous figure.
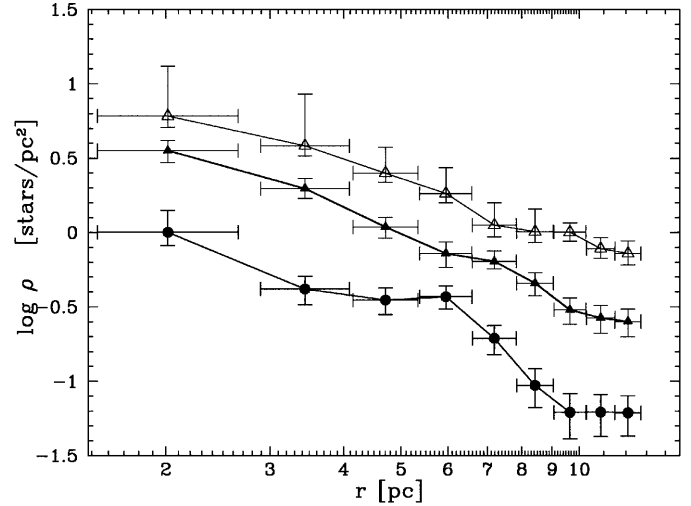

Fig. 12. Radial profile of stars of different masses. From top to bottom: open triangles, $7M_\odot < M < 10M_\odot$; filled triangles, $10M_\odot < M < 40M_\odot$; and filled circles, $M > 40M_\odot$.

0.07 while H96 quote $\Gamma = -1.01 \pm 0.07$ in the mass range $2.8M_\odot < M < 15M_\odot$ for this region, but give no explanation for the discrepant values of the slopes (see also Brandl et al. 1996, for a different analysis of the IMF and mass segregation in 30 Doradus combining a fraction of the H95 data with adaptive optics near-infrared observations).

We find $\Gamma = -1.37\pm0.10$ for $10M_\odot < M < 120M_\odot$ using only our data, in almost perfect agreement with a Salpeter slope. Fig. 11 shows the H95 and H96 counts together with ours. The IMFs merge smoothly given the errors, providing confirmation that the incompleteness and magnitude limit corrections have been properly determined. Combining our data with HST we find the slope over $2.8M_\odot < M < 120M_\odot$ to be $\Gamma = -1.17\pm 0.05$ using the H96 data, and $\Gamma = -1.25 \pm 0.05$ using H95.

3.2.2. Mass segregation

In Papers I and II we presented evidence for mass segregation in 30 Doradus in the form of a larger median distance to the cluster center for stars of smaller absolute luminosity. In this Paper we find an inner region IMF slope flatter than in the outer one, a 2-3σ effect, confirming the result from our previous work.

For $r < 5''$ our data are inconclusive and we must rely exclusively on HST. Although H95 and H96 do find evidence for a flattening of the IMF towards the core of the cluster, in their most recent HST work Massey & Hunter (1998a) deny the existence of mass segregation and ascribe the large number of very massive stars they observe in the core of the cluster to age effects. They base their conclusion on the fact that, extrapolating the *best fit* IMF of H96 for intermediate mass stars, they were able to predict exactly the number of massive stars ($50M_\odot < M < 120M_\odot$) they observed in the cluster core (22.8 stars predicted versus 23 stars observed within 2.8''of the

center). The flaw in this argument is that the *best fit* slope of H96, $\Gamma = -1.01$, is already flatter than the Salpeter slope which is observed elsewhere in the cluster, and which predicts ~ 2.5 times fewer massive stars in the core than they observed.

We conclude that mass segregation, as evidenced by a flattening of the derived IMF, is the most likely explanation for the large number of very massive stars present in the core of 30 Doradus. However, as we pointed out in Paper II, the HST spectra may be corrupted by nebular HeI lines and bad pixels which conspire to bias the data towards earlier spectral types.

Another way to investigate mass segregation is to compare the radial density profile of stars of different masses. The danger is that systematic errors due to crowding and incompleteness tend to mimic mass segregation. Figs. 10 and 11 show that for $M > 7M_\odot$ and $r > 15''$, and for $M > 10M_\odot$ and $r > 5''$ systematic errors are below 10% so we can confidently use these stars to study the density profiles. Fig. 12 gives the radial density profile, corrected for incompleteness and magnitude limit effects, for stars in 3 different mass bins. Below $40M_\odot$ the profiles are remarkably similar, while there is an excess of stars with $M > 40M_\odot$ between 4 pc and 8 pc. This excess of bright stars can be seen by eye in Fig. 7 around the 25'' circle (6 pc shell). What cannot be seen in this figure is that the number of less massive stars in the 6 pc shell does not show an equivalent increase. A χ^2 test rejects the hypothesis that the two sets of counts are drawn from the same distribution at the 98% confidence level. In the three radial bins centered at 6 pc shell one expects about 40 stars while $\sim$80 are observed. There is marginal evidence that the density of massive stars increases more rapidly towards the center, but the errors are too large to make this a firm conclusion.

3.2.3. The upper mass cut-off (M_U)

It has been claimed that M_U is not well defined, but is given by the stochastic nature of the IMF (Elmegreen 1997). Other

authors claim that there are physical reasons to expect a limit for the maximum mass of a stable star (Stothers 1992 and references therein). Perhaps the two ideas are not incompatible and the IMF is set by a random sampling of a fractal cloud, while physical process trim the over massive proto-stars to stable sizes leading to an IMF with an excess of stars with masses near the physical upper mass limit. This could result in a top-heavy IMF without need to invoke mass segregation. However, it is easy to show that this effect would increase the number of the most massive stars at most by a factor of 1.4 for a Salpeter slope, still significantly less than the factor of 2.5 needed to reconcile the HST counts with a Salpeter IMF.

Stellar models (e.g. Stothers 1992) predict that the most massive stable stars should have masses around $120M_\odot$ for solar metallicity, and $90M_\odot$ for SMC metallicity. This would imply an upper mass cut-off of about $100M_\odot$ for the LMC in apparent contradiction with our observations. In Fig. 4, the brightest stars are almost a whole magnitude more luminous than the $120M_\odot$ models, indicating that either the models are not accurate for these high masses, or that there are stars with larger masses, possibly binaries. We should point out that the Geneva tracks we used do not include the effects of mixing and rotation. For a given mass, models with rotation evolve at higher luminosities (Langer 1992) and are stable for larger masses (Stothers 1974).

From our observations alone, therefore, we conclude the most probable upper mass limit in the LMC is about $130M_\odot$.

3.2.4. The lower mass cut-off (M_L)

Our data does not go deep enough to provide a direct determination of the lower mass cut-off of the IMF, but it does allow us to understand the systematic errors that may mimic a low-mass cut-off in the photometry of massive young clusters.

As discussed above, the biggest offender is the *magnitude limit effect.* Fig. 10 shows that after correcting for incompleteness only, the 30 Dor IMF drops sharply at $\sim 6M_\odot$. In the inner region (Fig. 11), the effect is even more pronounced and starts at $\sim 15M_\odot$. But, when the magnitude limit correction is applied, the data are very well fitted by a single power law over the full mass range sampled with no evidence for a turn-over.

Nota (1998) has presented an IMF based on HST data that drops below $2M_\odot$. At $2M_\odot$ we expect V=20.0 unreddened so, in order to avoid magnitude limit corrections, the photometry must be complete to *at least* V=23.0. Although they claim to reach $V = 24.7$ (Siriani et al. 1998), it is not clear to which limiting V magnitude they determined the incompleteness correction over the area and color range of their study. The magnitude-limit correction starts to be important for the same mass bins for which the incompleteness correction starts to matter. Therefore, the claimed cut-off at $2M_\odot$ is very likely to be due to the magnitude-limit effect.

3.3. The radial density profile of the cluster

Fig. 13 shows the radial surface number density profile of the cluster. It combines the H96 data together with our counts cor-
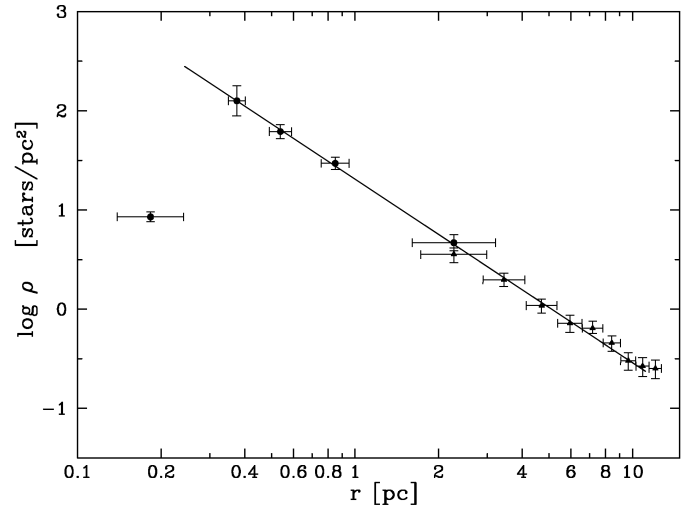

Fig. 13. Radial density profile for the stars with $10M_\odot < M < 40M_\odot$. For the innermost bins we have calculated the points using the Hunter et al. (1996) data following the procedure described in the text. The line is a power law with exponent -2.85.

rected for incompleteness and magnitude limit. We have restricted our counts to $10M_\odot < M < 40M_\odot$, and merged with the H96 counts by fitting a straight line to each radial bin in their Table 4 and then integrating the fitted $\xi = \xi(\log M)$. We can see that their innermost bin is highly incomplete. The line represents the relations

$$\Sigma_n(R) = 20.6 \, \frac{\text{stars}}{\text{pc}^2} \, \left(\frac{1\text{pc}}{R}\right)^{1.85},$$

$$\rho_n(r) = 9.8 \, \frac{\text{stars}}{\text{pc}^3} \, \left(\frac{1\text{pc}}{r}\right)^{2.85},$$

where r is the distance to the cluster center (R136a1) in parsecs, R is the projected distance in parsecs, and Σ_n and ρ_n are the surface and spatial number densities. Integrating the appropriate relations we can estimate a total of 1350 stars with $10M_\odot < M < 40M_\odot$ interior to 20 pc. Assuming a Salpeter slope we estimate for the same region 8000 stars with $3M_\odot < M < 120M_\odot$. In this mass range the average stellar mass is $8.44M_\odot$, resulting in a total of mass of $68000M_\odot$ for the cluster. Changing M_L from $3M_\odot$ to $0.1M_\odot$ increases the total number of stars by a factor of 100, and the total mass by a factor of 4.

Several studies of the radial density profile of the inner regions of NGC2070 have been published in the past. Campbell et al. (1992) using aberrated WFPC HST observations give a power-law fit to the F336W surface brightness profile generated by integrating the stellar photometry in concentric annuli. Their data is well modeled by a single power-law between $0.4'' < R < 4''$, with an exponent of 1.72 ± 0.06. They detect no core, and set an upper-limit of $R_c < 0.25''$. De Marchi et al. (1993) also measure the surface brightness distribution with the aberrated HST but integrating directly from the frame to avoid completeness limit issues. For $R > 1.7''$ their data are well represented by a power-law with index -1.9 while for $r < 1.7''$ their data shows an abrupt change of slope to a value

of -0.8. However, this flatter slope is probably due to a few off-center, very bright, W-R and O stars. Malumuth & Heap (1994) assign masses to the stars with a photometric method and fit a King model to the surface mass density profile. Ignoring their highly uncertain point at $0.1''$, their data is well represented by a power-law of slope -1.7. The WFPC2 HST work of Hunter et al. (1995) also shows a surface brightness profile which is well fitted by a power law of index -2, but they report an upper limit for the core radius of $R_c < 0.25''$. Brandl et al. (1996) present a profile based on adaptive optics near IR observations; From their Fig. 15 we determine a slope of -1.9 for the surface mass density profile for $R > 0.6''$. These authors find a core radius which increases with decreasing mass, but unfortunately this is the same effect one would expect by a failure to apply the magnitude limit correction, which they do not appropriately consider.

The mass density profile therefore, appears to be well determined and to be much steeper than an isothermal R^{-1} profile (projected). This is probably the result of the young age of a cluster which is not totally relaxed. This would explain the 6 pc shell of stars described above where an excess of high mass stars was detected since the bump in the density profile would have been erased had relaxation been completed. The offset between the center of the 6 pc shell and the center of the cluster, $\approx 1\,\mathrm{pc}$, provides further evidence that this stellar system is not yet relaxed. Restricting an isothermal or a King distribution function to contain only radial orbits (extreme case of anisotropy) leads to density profiles that have asymptotic slopes between -2 and -3 (see e.g. Lynden-Bell 1973). This happens because the de-population of the small eccentricity orbits has a larger effect in decreasing the density at larger radii. Because NGC2070 is such a young cluster its steep density profile could be evidence that it still remembers initial conditions of collapse.

4. Conclusions

1. A new photometric method was designed that allows the determination of masses for even the most massive stars from UBV photometry alone without introducing biases towards smaller masses. As a check of the method we obtained a distance modulus of $(m-M)_0 = 18.45 \pm 0.15$ for 30 Doradus in excellent agreement with the best estimate for distance to the LMC, $(m-M)_0 = 18.50$.
2. For $M > 20M_\odot$ we find the reddening distribution to be independent of stellar mass. The data are not complete to allow an accurate determination of this distribution below $20M_\odot$. We find a different reddening distribution for the stars near the center of the cluster (larger reddening close to the center) confirming the conclusions from Paper I. If not considered, this differential reddening distribution could introduce serious systematic effects in the IMF.
3. We have uncovered a systematic effect due to variable reddening which is responsible for the flattening of the IMF close to the limit of the photometry and we have designed

and applied a method to correct for this effect which we call *the magnitude-limit correction.*
4. We use our data to constrain the ages of stars with $M > 20M_\odot$, and find that the star-formation history is dominated by three bursts of increasing strength occurring 5My, 2.5My, and $\lesssim$1.5My ago. The number of high mass stars produced in each burst are approximately in proportion to the intensity of the burst, supporting Elmegreen's (1997) *stochastic sampling* interpretation of the IMF (with the exception of the somewhat flatter core and the 6 pc shell discussed below). The three bursts appear to be spatially disjoint with the youngest stars concentrated towards the center while the 2.5My stars appear to delineate a spherically symmetric structure of 6 pc radius slightly off-center. The observations are consistent with a picture where star formation propagated inwards in the cluster. The shell at 6 pc indicates a very complex structure for the ISM before the starburst.
5. For $r > 15''$ we find the IMF to be well represented by a power law with $\Gamma = -1.37 \pm 0.08$ for $3M_\odot < M < 120M_\odot$ consistent with the Salpeter slope. For $4.6'' < r < 19''$ and $10M_\odot < M < 120M_\odot$ we find $\Gamma = -1.37\pm0.10$. Combining our data with published HST observations we find $\Gamma = -1.25\pm0.05$ and $\Gamma = -1.17\pm0.05$ in this region, somewhat flatter than Salpeter. We reanalyze the Massey & Hunter (1998a) data and conclude, at variance with those authors, that the large number of O3 stars they observed in the core is not consistent with a Salpeter slope, and it is most likely due to a flattening of the IMF. The concentration of the most massive stars towards the center, irrespective of their ages, indicates that dynamical effects probably play an important role in shaping the spatial variations of the IMF.
6. The spatial density profile between 0.4 pc and 6 pc is well represented by a single power law with slope -2.85, steeper than isothermal. The density profile also shows an excess of stars within the 6 pc shell. Moreover, this shell appears to have a larger than normal proportion of high mass stars, providing evidence that Elmegreen's (1997) simple stochastic picture of star-formation is not the only mode at work in this complex region. The steeper overall profile of the cluster, together with the features in the density profile in the outer radial bins, indicates that the cluster is not relaxed, and that it might still have memory of its collapse.
7. We find that, if current evolutionary models are correct, there is evidence that the upper mass cut-off of the IMF is larger than 120M$_\odot$. It appear that the most massive stars in 30 Doradus have $M \approx 130M_\odot$, or that we are seeing the effects of rotation which for a given mass makes stars evolve at higher luminosities. Alternatively, the most massive stars in the cluster may all be binaries.
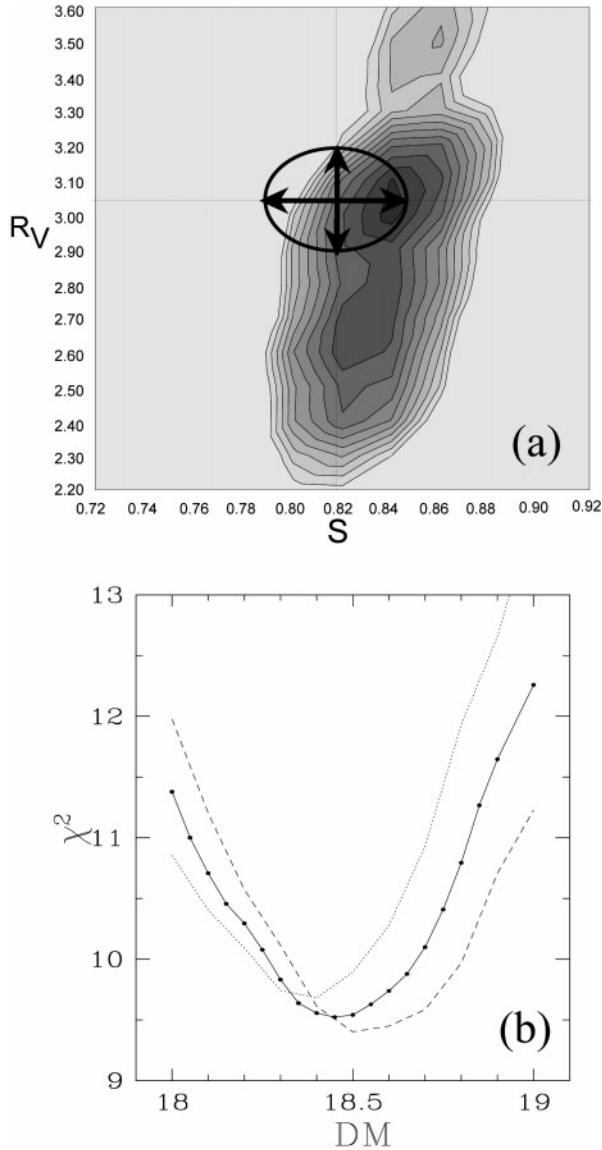
Fig. A1. a Photometric χ^2 map as a function of S and R_V. The ellipse marks the 1σ region around the best solution found in Paper I. **b** χ^2_{spec} as a function of the assumed $(m-M)_0$ to 30 Doradus. The curve for the best R_V value has a minimum at 18.45 magnitudes, in excellent agreement with previous determinations.

Appendix A: the distance to 30 Doradus

The performance of our Bayesian analysis of the CMS can be assessed by using it to determine the most likely values for $(m-M)_0$, S, and R_V. As explained in Paper I UBV data alone does not constrain R_V strongly. Nevertheless, it can be seen in Fig. A1a that both S and R_V determined photometrically agree with the values from Paper I. The best photometric values are thus S=0.84, $R_V = 3.05$.

Using $R_V = 3.05 \pm 0.15$ we find a true distance modulus of $(m-M)_0 = 18.45 \pm 0.15$ to 30 Doradus in excellent agreement with the best determined distance of $(m-M)_0 = 18.46 \pm 0.06$ to the LMC (Gieren et al. 1998).

References

Abraham R.G., 1999, In: Branes J.E., Sanders D.B. (eds.) Galaxy Interactions at Low and High Redshift. Kluwer, Dordrecht, p. 11
Abraham R.G., Tanvir N.R., Santiago B.X., et al., 1996, MNRAS 279, L47
Barnes J., 1998, astro-ph9811242
Barnes J., Hut P., 1986, Nat 324, 446
Bosch G., Terlevich R., Melnick J., Selman F.J., 1999, A&AS 137, in press (Paper II)
Brandl B., Sams B.J., Bertoldi F., et al., 1996, ApJ 466, 254
Brandt S., 1970, Statistical and Computational Methods in Data Analysis. North-Holland, Amsterdam
Campbell B., Hunter D.A., Holtzmann J.A., et al., 1992, AJ 104, 1721
Carpenter J.M., Meyer M.R., Dougados C., Strom S.E., Hillenbrand L.A., 1997, AJ 114, 198
Chlebowski T., Garmany C.D., 1991, ApJ 368, 241 (ChG)
Davis L.E., 1994, A reference Guide to the IRAF/DAOPHOT Package, NOAO
de Koter A., Heap S.R., Hubeny I., 1997, ApJ 477, 792
De Marchi G., Nota A., Leitherer C., Ragazzoni R., Barbieri C., 1993, ApJ 419, 658
Elmegreen B.G., 1997, ApJ 486, 944
Gieren W.P., Fouqué P., Gómez M., 1998, ApJ 496, 17
Glazebrook K., Ellis R.S., Colless M., et al., 1995, MNRAS 273, 157
Herbig G., 1962, ApJ 135, 736
Hunter D.A., Shaya E.J., Holtzman J.A., et al., 1995, ApJ 448, 179
Hunter D.A., O'Neil E.J., Lynds R., et al., 1996, ApJ 459, L27
Hunter D.A., Vacca W.D., Massey P., Lynds R., O'Neil E.J., 1997, AJ 113, 1691
Kendall M.G., Stuart A., 1977, The Advanced Theory of Statistics. Vol. 1, 4th edition, Charles Griffin, p. 212
Kurucz R.L., 1993, from ATLAS9 Stellar Atmospheres Programs and 2km s^{-1} Grid, CDROM13.COLORS, August 22, 1993, SAO
Langer N., 1992, A&A 265, L17
Lynden-Bell D., 1973, In: Contopoulos G., Henon M., Lynden-Bell D. (eds.) Dynamical Structure and Evolution of Stellar Systems. Saas-Fee 1973, p. 91
Malagnini M.L., Morossi C., Rossi L., Kurucz R.L., 1986, A&A 162, 140
Malumuth E., Heap S., 1994, AJ 107, 1054
Massey Ph., 1998, In: Gilmore G., Howell D. (eds.) The Stellar Initial Mass Function. Proceedings of the 38th Herstmonceux Conference, A.S.P. Conf. Ser. Vol. 142, p. 17
Massey Ph., Hunter D., 1998a, ApJ 493, 180
Massey Ph., Hunter D., 1998b, In: Howarth I. (ed.) Properties of Hot Luminous Stars. ASP Conf. Ser. 131, p. 355
Melnick J., 1985, A&A 153, 235
Melnick J., 1992, In: Tenorio-Tagle G. Prieto M., Sánchez F. (eds.) Star Formation in Stellar Systems. CUP, Campridge, p. 253
Meynet G., Maeder A., Schaller G., Schaerer D., Charbonnel C., 1994, A&AS 103, 97
Meyer M.R., 1996, Ph.D. Thesis, University of Massachusetts, Amherst
Mihos J.C., Hernquist L., 1994, ApJ 431, L9
Nota A., 1998, STScI Newsletter 15(4), 1
Parker J.Wm., Garmany C.D., 1993, AJ 106, 1471
Parker J.Wm., Garmany C.D., Massey P., Walborn N.R., 1992, AJ 103, 1205
Pettini M., Kellog M., Steidel C.C., et al., 1998, astro-ph/9806219
Press W.H., Teukolsky S.A., Vetterling W.T., Flannery B.P., 1994, Numerical Recipes in C: the art of scientific computing. Cambridge University Press

Salpeter E., 1955, ApJ 121, 161

Schaerer D., Meynet G., Maeder A., Schaller G., 1993, A&AS 98, 523

Schmidt-Kaler Th., 1982, In: Schaifers K., Voigt H.H. (eds.) Stars and Star Clusters. Volume 2b, part of the Landolt-Börstein series on Numerical Data & Functional Relationships in Science and Technology, chief ed. K.-H. Hellwege, Springer-Verlag, Berlin-Heidelberg, p. 1 (SchK)

Selman F.J., Melnick J., Bosch G., Terlevich R., 1999, A&A 341, 98 (Paper I)

Siriani M., Nota A., Leitherer C., Clampin M., De Marchi G., 1998, In: Howarth I. (ed.) Properties of Hot Luminous Stars. ASP Conf. Ser. 131, p. 363

Stahler S., 1985, ApJ 293, 207

Stetson P.B., 1997, The *Daophot II* User's Manual

Stothers R., 1974, ApJ 192, 145

Stothers R., 1992, ApJ 392, 706

Tolstoy E., Saha A., 1996, ApJ 462, 672

Vacca W.D., Garmany C.D., Shull J.M., 1996, ApJ 460, 914 (VGS)

Walborn N.R., Blades J.Ch., 1997, ApJS 112, 457

Walborn N.R., Parker J.Wm., 1992, ApJ 399, L87